Ultra-short and highly efficient metamaterial Fresnel lens-assisted taper

Pascar, Leonid; Xu, Dan-Xia; Grinberg, Yuri; Sajjanam Morrison, Sunami; Vachon, Martin; Liboiron-Ladouceur, Odile

Publisher's version / Version de l'éditeur:
https://doi.org/10.1364/OE.531098
Optics Express, 32, 16, pp. 1-14, 2024-07-23

Research Article | Vol. 32, No. 16 / 29 Jul 2024 / Optics Express 28522
Optics EXPRESS

Ultra-short and highly efficient metamaterial Fresnel lens-assisted taper

LEONID PASCAR,[1,*] DAN-XIA XU,[2] YURI GRINBERG,[3] SUNAMI SAJJANAM MORRISON,[1] MARTIN VACHON,[2] AND ODILE LIBOIRON-LADOUCEUR[1]

[1]Department of Electrical and Computer Engineering, McGill University, Montreal (QC), Canada
[2]Quantum and Nanotechnologies Research Center, National Research Council Canada, Ottawa (ON), Canada
[3]Digital Technologies Research Center, National Research Council Canada, Ottawa (ON), Canada
[*]leonid.pascar@mail.mcgill.ca

Abstract: This paper demonstrates the benefits of leveraging free-space optics concepts in the design of certain integrated photonic components, leading to a footprint reduction without compromising on performance. Specifically, we present ultra-short, highly efficient and fabrication-friendly mode-size converters based on metamaterial Fresnel lens-assisted tapers. This is achieved using a parameterized inverse-design approach, where the metamaterial phase shifters are realized using fabrication-friendly Manhattan geometries, by optimizing the width, length, and position of the phase shifters. This approach overcomes the limitations of the conventional method that uses local periodic approximation, which is not suitable for lenses with a short focal length and high numerical aperture. We also extend the free-space concept of compound lenses and demonstrate a doublet-based taper to further reduce the footprint. The devices are fabricated and experimentally characterized in terms of insertion loss and signal integrity at high data transmission rates, exhibiting high performance. For the singlet, it effectively achieves mode-size conversion from 15 μm to 0.5 μm within a 15 μm distance, leading to ×10 length reduction compared to a linear taper. The insertion loss is under 1 dB over the entire C-band. The doublet achieves the same mode-size reduction within a 10 μm distance, leading to ×15 length reduction compared to a linear taper. The insertion loss is near 1 dB over most of the C-band. In both cases, the signal integrity is maintained for up to 50 Gbit/s.

1. Introduction

Silicon photonics is a promising technology that is used in industry and in academic research for a variety of applications such as communication, sensing and computing [1–3]. As of now, the high refractive index contrast between silicon and silica allows for a good degree of miniaturisation of photonic devices. To allow for denser integration, however, further reduction in the device footprint is required [1]. In this context, the incorporation of free-space optics techniques into integrated photonics can generate complementary solutions. This approach is yet to be widely used in silicon photonics, but it has the potential to pave the way for further on-chip photonic miniaturization [4].

In this paper, we demonstrate an on-chip wavefront manipulating device. Taking inspiration from the free-space optics techniques we implement a mode-size converter by embedding a Fresnel lens in an ultra-short taper. Such a Fresnel lens-assisted taper offers a significant reduction in footprint compared to linear adiabatic tapers [5] while retaining robustness to fabrication, as shown in Fig. 1. Figure 1(a-c) depict the adiabatic taper, the singlet (a one lens system) and the doublet (a two lens system) all drawn to scale, emphasizing the length reduction. Figure 1(e, d) show close-up images of the lenses, along with illustrations of their corresponding free-space lens-based equivalents in Fig. 1(f, g). Such mode-size converters are particularly relevant in the

#531098 https://doi.org/10.1364/OE.531098
Journal © 2024 Received 28 May 2024; revised 10 Jul 2024; accepted 14 Jul 2024; published 23 Jul 2024

Optics EXPRESS

case of uniform grating couplers (GCs) that couple optical fields from fibers carrying multi-modes or dual polarizations and with a large mode-size, like the one of SMF-28, which is then transferred into a single mode waveguide of approximately 500 nm in width. In such cases, the commonly used curved focusing gratings are not easily implemented. Further, we adopted the compound lens concept common in free-space optics, wherein an assembly of lenses serve as a single focusing unit. This arrangement is widely used to compensate for aberrations [6–8] by inducing an adiabatic ray refraction. Figure 2 illustrates a schematic of a case where a doublet corrects for the aberrations of a singlet. The singlet for short focal length or high numerical aperture, on the left, fails to focus all the rays to a single meeting point due to those aberrations. The doublet, on the right, manages to do so because the two lens system allows more moderate refraction angles.

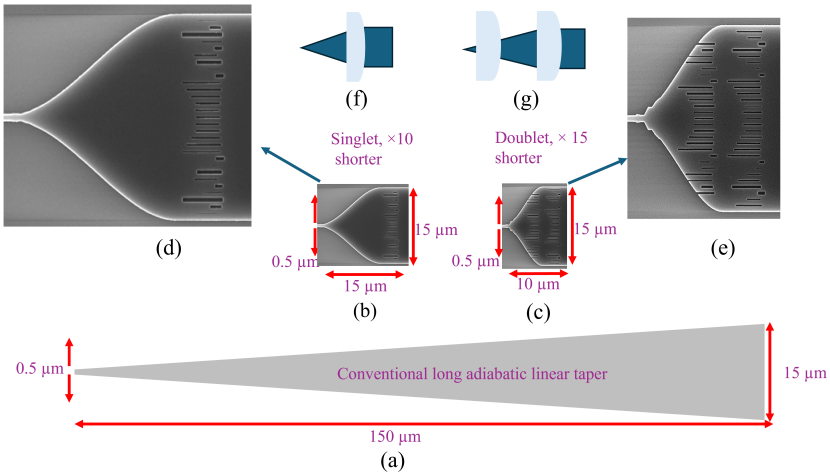

Fig. 1. Illustration of the significance of lens-assisted tapers (singlet and doublet) footprint reduction compared to adiabatic linear taper. In the bottom part, (a) linear taper, (b) singlet-assisted taper and (c) doublet-assisted taper are drawn to scale. In the top part, there are close-up images of (d) the singlet and (e) the doublet and their equivalent free-space illustrations of (f) the singlet lens system and (g) the doublet lens system.

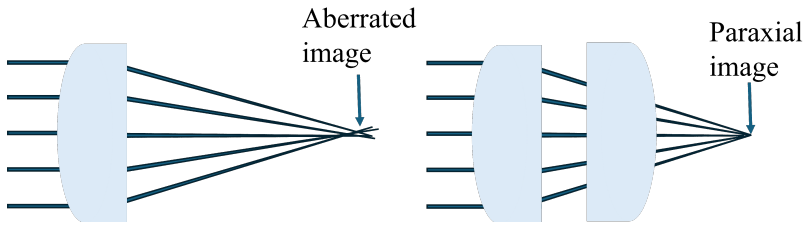

Fig. 2. Free space optics example of how a doublet can compensate for aberrations (not to scale). In the case of short focal length or high numerical aperture, the singlet does not focus all the rays to the same point, while the doublet manages to do so.

The on-chip lenses are built using metamaterials. These are sub-wavelength arrays tuned to engineer the required phase, amplitude and polarization response applied to incoming field distribution [9,10]. In recent years, there have been many demonstrations in silicon photonics of metamaterial-based devices for diverse applications [11] such as multiplexers [12,13], edge couplers [14,15] and multi-mode interferometers (MMI) [16,17]. There is also a recent demonstration of an integrated parabolic mirror lens that takes inspiration from free-space

Optics EXPRESS

optics for performing mode-size conversion [18]. Our designs use rectangular silica slots etched inside a silicon slab waveguide to engineer the lens phase response. The size and location of a slot induces a corresponding local phase delay. Therefore, the slots can be referred to as phase shifters. An ensemble of phase shifters are optimized to produce the desired phase modification.

The conventional design approach to developing integrated metamaterial lenses often relies on local periodic approximation [19], i.e. it assumes that the response of each phase shifter is the same as in a periodic structure with its exact duplication. Hence, the amplitude and interaction between dissimilar adjacent phase shifters (that induce a different response) are disregarded [20]. This design method is prone to high aberrations for lenses that have ultra-short focus/high numerical aperture (NA) (the range of angles that the lens can accept light). Ultimately, the performance degradation in terms of insertion loss can be significant. Another approach that has been tried to improve upon this limitation is topological inverse-design [21] to account for the varied near-field interaction between adjacent slots. However, this pathway produces arbitrary shapes, often with small features that may violate design rules and are, in general, more prone to process variations.

To design ultra-short focus/high NA lenses, we present a parameterized and physics informed inverse-design methodology. Herein, the shape of the phase shifters is restricted to rectangles while the length, width, and position along the propagation axis are optimized. This produces a geometry which not only yields high performance but is also robust to process variations - an important requirement in the silicon photonics industry. To demonstrate our methodology, we design, fabricate, and experimentally verify three singlet-assisted tapers and one doublet-assisted taper, offering varying values of focal length. The first two singlets convert fundamental transverse electric mode (TE0) from a 9.5 μm-wide waveguide to a 0.5 μm-wide waveguide, over a length of 8 μm and 11 μm respectively. The third singlet converts light from a 15 μm-wide to a 0.5 μm-wide waveguide over a length of 15 μm. To demonstrate their utility, the lenses are connected to a pair of uniform GCs that coupled SMF-28 fiber field to a photonic integrated circuit (PIC), and yield a mode conversion loss of $\leq$ 1 dB over the C-band. This result is comparable to a 150 μm-long adiabatic linear taper. The doublet-assisted taper converts light from a 15 μm-wide to a 0.5 μm-wide waveguide over a shorter distance of 10 μm. The coupling, near 1 dB for most of the C-band, is also comparable to a 150 μm-long linear taper.

Notably, insertion loss is not the only parameter of interest in silicon photonics and optical communication. Signal integrity at high data bit rates is critical for the device to be considered for system integration. Therefore, we characterize the fabricated devices in terms of eye diagrams and signal-to-noise ratio (SNR). Those measurements verify that the signals do not experience degradation at 50 Gbit/s data rate, which is the limit of our testing setup.

2. Design

Our objective is to achieve mode-size conversion from a wide waveguide to a narrow waveguide over a given length using an integrated metamaterial Fresnel lens, which has a desired phase distribution as shown in Fig. 3(a). This concept is based on a sub-wavelength array of phase shifters that are realized by embedding rectangular silica slots inside a silicon slab waveguide. The rectangular slot shapes ensure that minimum feature size constraints are easily enforced. The rectangle's dimensions control the local effective refractive index due to material index contrast. Large and small slots introduce high and low contrast, respectively, to the surrounding silicon. This translates into phase retardation, since oxide has a lower refractive index than that of silicon. Therefore, by sampling the required phase response $\phi\,(y)$ of the lens (Eq. (1) for a given focal length f, wavelength λ and coordinate y) at a pitch that satisfies the subwavelength condition (to suppress the Bragg diffraction), the lens phase response can be synthesized by rectangular slots,

Optics EXPRESS

as illustrated in Figs. 3(a) and 3(b).

$$\phi(y) = \frac{2\pi}{\lambda} * (\sqrt{y^2 + f^2} - f^2) \tag{1}$$

Phase propagation in the core resembles the free-space focusing of a plane wave, as shown in Fig. 4. The wavefront, in the wide waveguide is flat (plane wave-like), and the one in the taper resembles a converging spherical wave. The design methodology is comprised of a physics-guided initialization of the taper parameters and then followed by parameterized inverse design optimization. First, the response of a periodic array of a phase shifter of a given width is computed as a function of length. An initial metamaterial lens-assisted taper is then generated where the difference in interaction between adjacent dissimilar phase shifters is ignored. The phase response (or the length) of each phase shifter is determined by the spatial phase distribution which corresponds to the focal length of interest. Then, parameterized inverse-design optimization is executed where the length, width, and position (along the focusing direction), as shown in the close-up of Fig. 3(b), of each slot are modified to optimize the coupling of TE0 using finite-difference time-domain (FDTD) simulations. This procedure allows bypassing the limitations of the local periodic approximation. This methodology is applied both to the singlets and the doublets, first using 2D FDTD to set the initial condition, then further optimized using 3D FDTD on most promising designs.

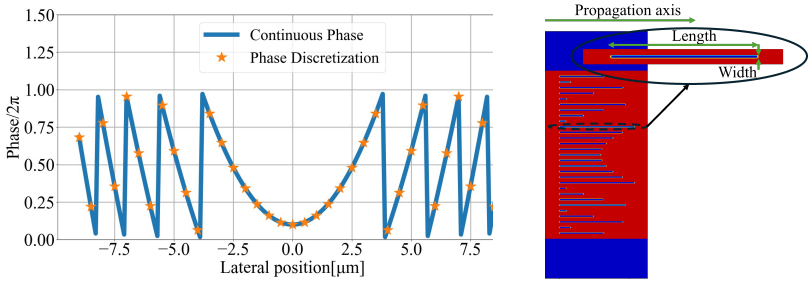

Fig. 3. (a) Discretization of the lens phase response, (b) implementation by metamaterial phase shifters and a close-up of a phase shifter and description of its parameters. Red is silicon, and blue is silica.

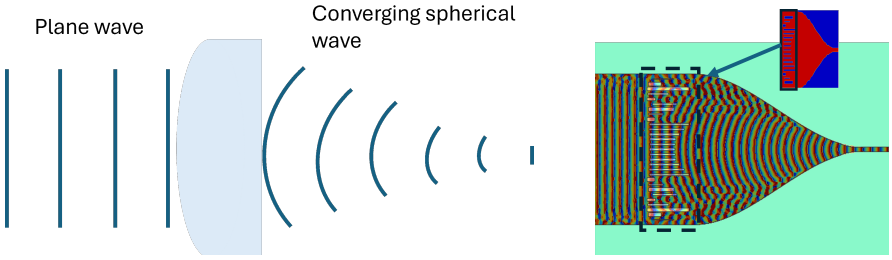

Fig. 4. Phase manipulation of (a) conventional free-space lens and (b) integrated metamaterial lens. The phase at the cladding is set to zero.

All generated lenses are designed as Fresnel lenses, i.e., the phase difference is in the range of 0-2π, as shown in Fig. 3(a). This limits the length of the phase shifters and keeps the design more compact especially in the case of short focal and wide aperture. In the following section,

Optics EXPRESS

we outline the physics-informed initial structure, the rationale for the chosen degrees of freedom (DOF), the inverse-design optimization, and our motivation behind the doublet.

2.1. Physics informed initial conditions

The initial conditions determine the geometry that the optimizer receives as an input. In this design, it relates to the shape of the metamaterial phase shifters and the taper boundary geometry. The waveguides are on a silicon-on-insulator platform with 220 nm thick silicon embedded in silica, with effective refractive index of 2.847 and 1.444 respectively in 2D simulations. The initial meta-lens structure is designed according to the conventional method which comprises of the following steps:

1. Choose a phase shifter pitch that satisfies the sub-wavelength condition, and a width. The chosen values are 0.5 μm and 0.14 μm, respectively (see Fig. 3). The chosen values provide good phase sampling and are above the fabrication minimum feature size.

2. Calibrate the phase versus length of the phase shifters in a periodic array. This is obtained by applying periodic boundary conditions in 2D FDTD simulations (as the initial optimization is in 2D), where we iterate over the length of each rectangular slot for the width and period values of step 1, and record the corresponding phase. The zero phase length $Length_0$ is set to 200 nm and the extracted (for this calibration) 2π length $Length_{2\pi}$ is 3.2 μm. The overall linear phase response $\phi\ (L)$ versus phase shifter length L is described by Eq. (2)

$$\phi(L) = \frac{2\pi}{Length_{2\pi} - Length_0} * L \tag{2}$$

3. Choose the focal length f that corresponds to the desired mode-size conversion length. This determines the required spatial phase response of the lens.

4. Sample the required phase response by a period that is equal to the phase shifter pitch. Each sampled point determines the required phase response of each phase shifter. The phase in Fig. 3(a) is sampled at a pitch of 0.5 μm. Each sampled point corresponds to a phase shifter in Fig. 3(b).

5. Set the phase shifters' length according to the sampled values and the calibration (from step 2).

6. Iterate over a few focal lengths f to have the best possible initial structure with the lowest coupling loss to TE0 since the mode-size conversion length is not necessarily equal to the focal length. This is particularly pronounced for compound lenses such as the doublet, where the distance between the lens and the focal plane can differ significantly (in the scale of a few micrometers) from the focal length.

Although it is possible to perform inverse-design optimizations using random initialization, we have investigated and demonstrated that optimizations with physics informed initial conditions, instead, show better performance in terms of insertion loss and computational time. We examined a case study of 2D optimization of mode-size conversion from a 9.5 μm-wide waveguide to a 0.5 μm-wide waveguide over a length of 8 μm. Multiple executions of optimization with random initialization converged to a higher insertion loss (in the scale of 0.5 dB or more) over more iterations, compared to physics informed initial conditions.

Optics EXPRESS

2.2. Inverse design optimization

The conventional approach, which relies on local periodic approximation, neglects the effect of dissimilar adjacent phase shifters. The deficiency of this assumption is particularly pronounced in lenses with short focal lengths and high NA as the phase changes quickly across spatial locations. Consequently, this approach is unable to compensate for high aberrations due to the inaccurate phase response calibration. Moreover, for Fresnel lenses, the 2π period is shorter. Therefore, unsurprisingly, the insertion loss of the initial meta-lens structure is on a scale of 2-3 dB.

To improve upon the performance of initial meta-lens structure we use a parameterized inverse design methodology. It tackles the challenges posed by optimizing the complete structures that are described by complex and non-analytical physics, using FDTD simulations. In this case, two problems are addressed. First, the coupling between dissimilar phase shifters, especially for rapid phase variations, is included. Second, the interactions between the phase shifters and the waveguide core boundaries are now included. The length calibration step assumes slots embedded in a slab waveguide with periodic boundary conditions according to the local periodic approximation. The calibration does not take into account that the slab width is finite. The finite slab width affects the local field distribution at the phase shifters that are close to the waveguide core boundary. It is important to note that the latter is relevant only in integrated photonics where the meta-lens is embedded within the waveguide. This is not the case for free-space metamaterial lenses set in ambient air. The inverse design optimization reduces the insertion loss to 1 dB or less (depending on the design), without having to develop any explicit or implicit physical model.

Previous work optimized only the length of the slots [22] or performed topological optimization within the slots' boundary [21] where the optimizer is allowed to design arbitrary shapes. We found that the former is insufficient to compensate for the many aberrations in the case of an ultra-short focal length and high NA, while the latter produces geometries with finer features which, in some cases, violates the fabrication process design rule about the minimum size of features. Moreover, there are more regions of finer features and curvatures compared to a rectangular phase shifter. This increases the sensitivity of each slot to random process variations. In general, it is possible to perform topological inverse-design, and then enforce strict fabrication constraints [23]. However, this multi-step topological optimization process is relatively complex and often requires parameter tuning such as the penalty function coefficients. Enforcing the fabrication constraints in the topological optimizer often degrades the performance as well. This makes topological optimization within the slots' boundary more difficult to fabricate with high fidelity, limiting their potential of being integrated as part of a deployed practical system. Our rectangle parameterized approach avoids some of those complexities by applying bounds on the possible width and length values of the phase shifters.

We also investigate the effect of optimizing the taper boundary and its relation to the DOF of the metamaterial phase shifters in terms of insertion loss and fabrication-friendly geometry. In this case, we allow the variation of the vertical coordinates of the vertices (spaced horizontally 0.3 μm apart) on the taper boundary. Two scenarios are compared: (1) only the length of the phase shifters is optimized (one DOF); (2) the length, width, and the position along the field propagation direction are all optimized (three DOF). The latter not only yields superior performance (a 0.25 dB insertion loss improvement), but also produces a smoother taper-boundary geometry. As seen in Fig. 5, the taper boundary geometry is expected to be less sensitive to fabrication deviations for the case with three DOF, as compared to when only the end of the taper boundary has been changed. We investigate the effect of the width variation to understand its contribution. Therefore, we extract the phase versus length response for three different slot width values as shown in Fig. 5(c). The phase changes moderately and rapidly for narrow and wide widths, respectively. In the three DOF case, the optimization results in narrow widths close to the center, probably to accommodate for the required slow phase changes. Further from the center, the required changes are quicker and the optimized width is wider as well. The changes in width allow

Optics EXPRESS

various degrees of phase tailoring resolution necessary for compensating the aberrations. The position parameter adds another DOF for building the desired wavefront. It is worth noting that the transmittance has a periodic dependence on the phase shifter length. While this dependence becomes stronger with larger width, the same high transmittance is achievable by the optimizer for any width by optimizing the length. With the width-dependence transmittance for a given phase shifter length, the optimizer, thus, finds the optimum length and width that provide the required phase while maintaining high transmittance. Overall, these optimization results show that optimizing length, width, and position leads to better optical performance and significantly lessens the need to adjust the taper's boundary. Therefore, all the devices are optimized with those three parameters for each slot.

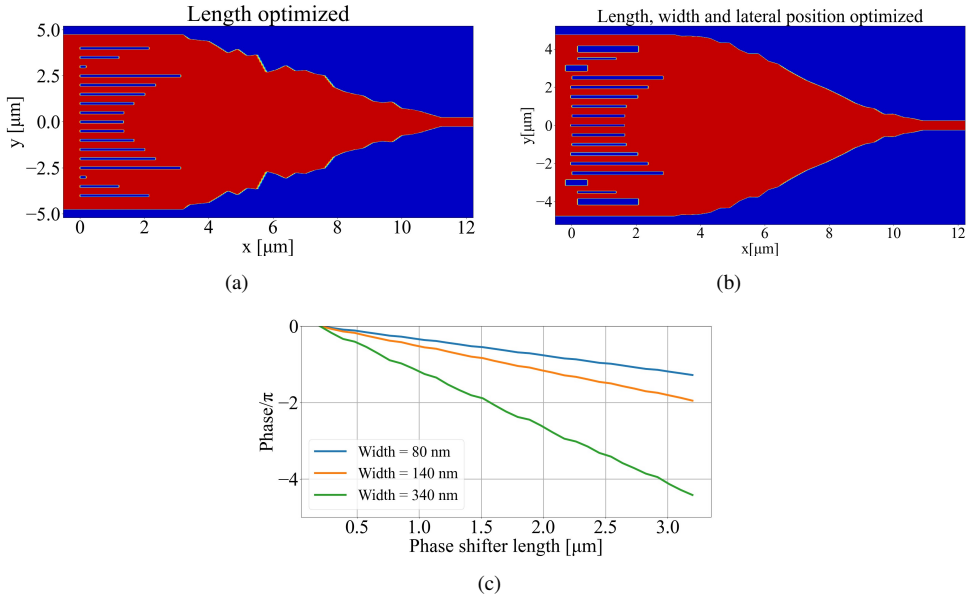

Fig. 5. The effect on the taper boundary shape when (a) only the length is optimized and (b) length, width and lateral position are optimized. Silicon is red, and silica is blue. (c) Phase response for different slot widths at a pitch of 0.5 μm.

As demonstrated above, the requirement of the taper's boundary geometry is relaxed in the case of the three slots' parameters optimization. Yet, optimizing the taper's end prevents an abrupt discontinuity of the field in the transition region between the taper and the narrow waveguide. Therefore, we optimize the y coordinate of the final three or four vertices (depending on the design case), spaced 0.3 μm apart.

2.2.1. Technical description of the optimization

We use the inverse design platform Lumopt of Ansys/Lumerical FDTD solver, which uses the adjoint method to optimize the selected figure of merit (FOM), chosen as the coupling efficiency of the TE0 mode, according to a certain set of parameters within allowed boundaries. In this approach, the polygon boundary is directly parameterized [24] (by the width and the length parameters) instead of the topological inverse-design approach where the permittivity is optimized in each pixel of the design space. The parameterized optimization uses the permittivity gradients to calculate the gradients of the FOM with respect to the phase shifter dimensions, using the gradient chain rule calculation. To save computational resources, the first optimization is performed in 2D. The ones that perform well serve as initial conditions for 3D optimizations,

Optics EXPRESS

which are the computationally intensive parts. Therefore, we use structural symmetry to save memory and reduce computing time. To further save computational resources, different mesh-grids with varying resolutions are used in different regions. In important regions that contain the phase shifters and the end of the taper, a fixed grid with a resolution of 20 nm is used. In other parts, we employ a coarser non-uniform mesh type in Lumerical FDTD with a mesh accuracy of 2 (defined as low accuracy). We use the LumOpt optimization method based on the limited-memory Broyden-Fletcher-Goldfarb-Shanno bound (L-BFGS-B) algorithm [25]. The default hyper-parameters to establish the convergence, such as the change in FOM from the last iteration and the magnitude of the gradient vector, are not changed. Fig. 6 is an example of how the FOM changes during the optimization process for 2D and 3D optimizations for a mode-size conversion from 9.5 μm to 0.5 μm over a length of 8 μm. The 2D optimization starts with a physics-informed initialization at a coupling loss of 2.5 dB and converges to 0.25 dB. The coupling of the 2D optimized device is evaluated by the 3D simulation, resulting in 0.75 dB loss. This shows that 2D calculations are insufficient for an accurate insertion loss evaluation. Yet, it saves a lot of time as a 3D iteration takes four to eight times longer than a 2D iteration as presented in Fig. 6(b). In the 3D case, the starting point is with a reasonable coupling and the improvement is milder than the 2D, from 0.75 dB to 0.6 dB.

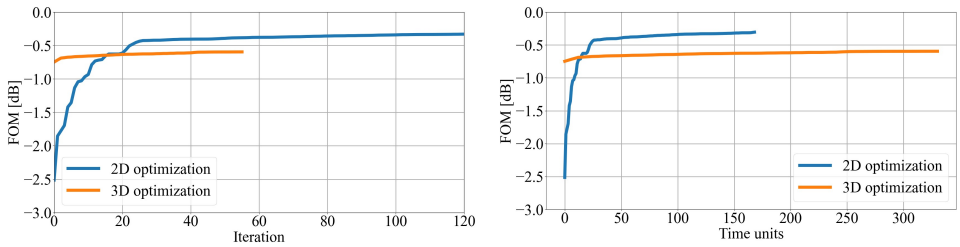

Fig. 6. Example of optimizations where the FOM (coupling to TE0) is optimized: (a) FOM versus number of iterations, and (b) FOM versus number of time units. The blue and the orange curves relate to the 2D and 3D optimizations respectively.

2.3. *Doublet design*

In free-space optics, it is often the case that to compensate for aberrations, a single lens functionality is implemented by an assembly of lenses as shown in Fig. 2. The ray-refraction angles here are moderate and the overall focusing process is adiabatic. This kind of adiabatic approach is shorter compared to an adiabatic linear taper. Therefore, the concept can be utilized in silicon photonics to further reduce the footprint of mode-size converters. Following this insight, we design a doublet-assisted mode-size converter. In the 2D case study of converting a mode from a 15 μm-wide waveguide to a 0.5 μm-wide waveguide, over a 15 μm-long taper, a doublet-based taper shows a 0.25 dB loss reduction compared to the singlet-based taper (0.5 dB loss). The insertion loss is extracted by applying the Euclidean norm to the field overlap integral calculation between the target field distribution in the narrow waveguide and the resulting output field distribution. The aberrations manifest themselves in the spatial phase distribution of the output field with higher degree of aberrations leading to a higher phase mismatch between the output field and the target field. This field mismatch leads to an increase in insertion loss. The lower insertion loss of the doublet indicates that the aberrations are reduced compared to the singlet. This improvement is enabled by the more moderate phase transition in the former than in the latter. To further reduce footprint, we chose to design a doublet to achieve mode-size conversion from 15 μm-wide waveguide to a 0.5 μm-wide waveguide, over a shorter

Optics EXPRESS

10 μm-long taper. The 2D optimization result is promising (0.55 dB coupling). However, due to computational resource limitations, we only ran a partial 3D optimization for the 10 μm-long doublet. Our computing platform did not have enough RAM memory (32 GB RAM and 12 cores) to perform a 3D optimization for a 15 μm-long doublet. The doublet setup approximately doubles the number of optimization parameters (91 versus 50) as there are more phase shifters. The gradient calculation is the bottleneck in terms of memory consumption and computing time in parameterized inverse-design optimization using the LumOpt platform. Therefore, the 10 μm-long doublet consumed more memory than the 15 μm-long singlet. A different optimization platform may enable performing 3D optimization for a longer device and improve the performance of the shorter one. The expected insertion loss for the 10 μm-long doublet is close to 1 dB for most of the C-band.

3. Fabrication and measurements

3.1. Uniform GCs and comparison to a 150 μm linear adiabatic taper

In some applications, fiber-to-PIC couplers use uniform GCs that require mode-size converters to match the received light to the waveguide field profile on chip. For instance, such GC is used in dual polarization [26, 27] and/or multi-mode couplers [28]. We focus on coupling SMF-28 field and converting it to typical 220 nm-thick silicon photonic single-mode waveguide in TE mode. In our experiment, the mode-size conversion is from a 15 μm-wide waveguide to a 0.5 μm-wide waveguide. We fabricated uniform GCs connected to 15 μm-long singlet lenses (Fig. 7), and 10 μm-long doublet lenses. We also fabricated uniform GCs connected to 150 μm-long adiabatic tapers to serve as a reference. The fabrication took place at Applied NanoTools (ANT) using the NanoSOI Fabrication Service (100 keV electron-beam lithography). Figure 8 shows the measurement setup, which includes a tunable C-band laser and a polarization controller (to set the polarization state). The measurement results are presented in Fig. 9, where three copies of the lens-based structures are shown and compared with the linear taper. The singlets are comparable to the adiabatic tapers both in terms of best insertion loss and bandwidth (though with a slight blue shift). The length is reduced by a factor of 10 with no additional insertion loss. In the case of the doublet, the best insertion loss is comparable as in the case of the former, but there is a slightly higher wavelength dependent loss as indicated in the simulation. The length of the mode-sized converter is reduced by a factor of 15 without compromising peak insertion loss. Moreover, in both figures there are only small differences between the loss curves for the lens-based mode-size converters. This demonstrates robustness to fabrication imperfections. In both cases, the uniform GCs contribute most to the loss. This is confirmed by the results of the lens loss reported in the next section. It is important to note that the uniform GCs are not optimized. The design is based on straightening the curves of ANT's focusing GC, i.e., the same groove period and duty cycle are used. The measured insertion loss of the uniform GC is in the same scale as the focusing GC.

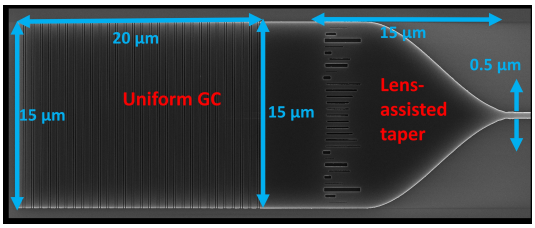

Fig. 7. SEM image of the fabricated 15 μm-long singlet mode-size converter and a uniform GC 15 μm-wide and 20 μm-long.

Optics EXPRESS

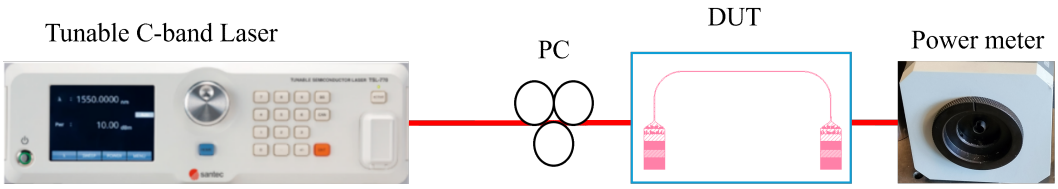

Fig. 8. Insertion loss measurement setup. PC: polarization controller, DUT: device under test.

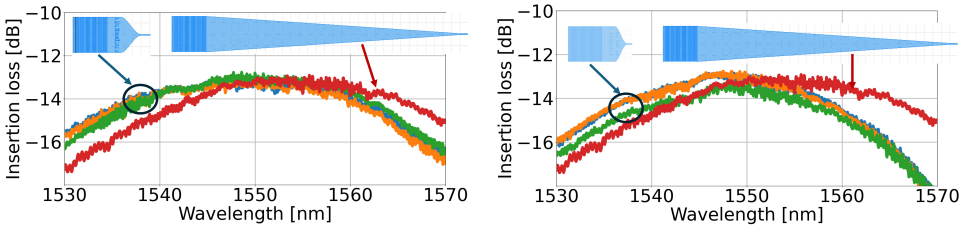

Fig. 9. Insertion loss for the loopback structures with (a) three copies of the singlet and (b) three copies of the doublet mode-size converters versus a 150 μm adiabatic linear taper. Most of the loss is due to the uniform GCs. Minor difference between the curves demonstrates robustness to fabrication.

3.2. *Lens insertion loss measurement*

We fabricated structures that include devices with changing numbers of cascaded back-to-back pairs of lenses (Fig. 10) to characterize the insertion loss for each designed lens and to demonstrate robustness to random fabrication variations. We obtained the power as a function of the number of lenses. The light is coupled via ANT's focusing GCs, instead of uniform GCs, to facilitate parallel comparison of lens-based tapers with varying widths. The narrow waveguide width is 0.5 μm for all cases. The fabricated lenses include three singlets and a doublet. The singlets convert the mode from 9.5 μm, 9.5 μm, and 15 μm-wide waveguides over a length of 8 μm, 11 μm and 15 μm, respectively. The doublet converts a mode from a 15 μm-wide waveguides over a length of 10 μm. The 15 μm singlet and the doublet are the same as those used in the previous section. The insertion loss at a given wavelength is extracted by applying a linear fit, per wavelength, in a dB scale. The results, indeed, show a strong linear relation, indicating that the loss values do not vary significantly. This indicates that the lenses are robust to process variations within a single chip. For the singlet lenses, the measured insertion loss values are in agreement with the simulated values, showing a nearly flat < 1 dB loss over the entire C-band (Figs. 11(a), 11(b), 11(c)). For the singlets with a width of 9.5 μm, the 11 μm-long lens has a better insertion loss by 0.2 dB relative to the 8 μm-long lens as reducing the mode conversion increases the NA and the insertion loss. With regard to the doublet, Fig. 11(d) shows a slight wavelength dependence and a higher loss at the C-band boundary, in agreement with the simulation. The power drop at 1567 nm can be attributed to the lens characterization setup rather than to the device itself. When the device is used with the uniform GC test structure, there is no power drop. This indicates that the power drop in the lens characterization setup is due to the cavity-resonance effect between the two back-to-back lenses in the lens-pair and not the device itself.

Optics EXPRESS

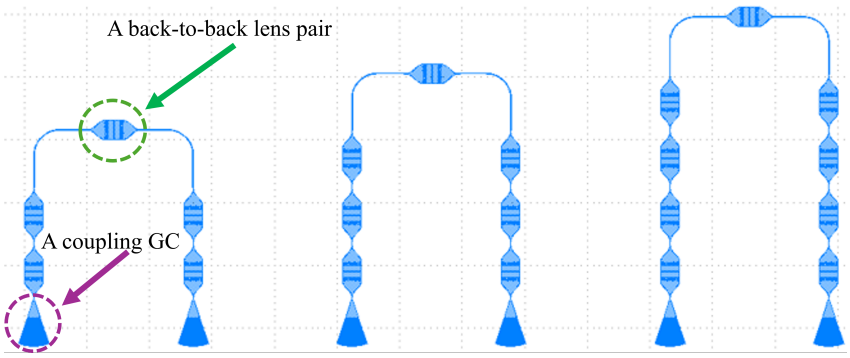

Fig. 10. Illustration of insertion loss characterization structures with changing number of cascaded lens-pairs. On the DUT, the number of lens-pairs changed from one to 19.

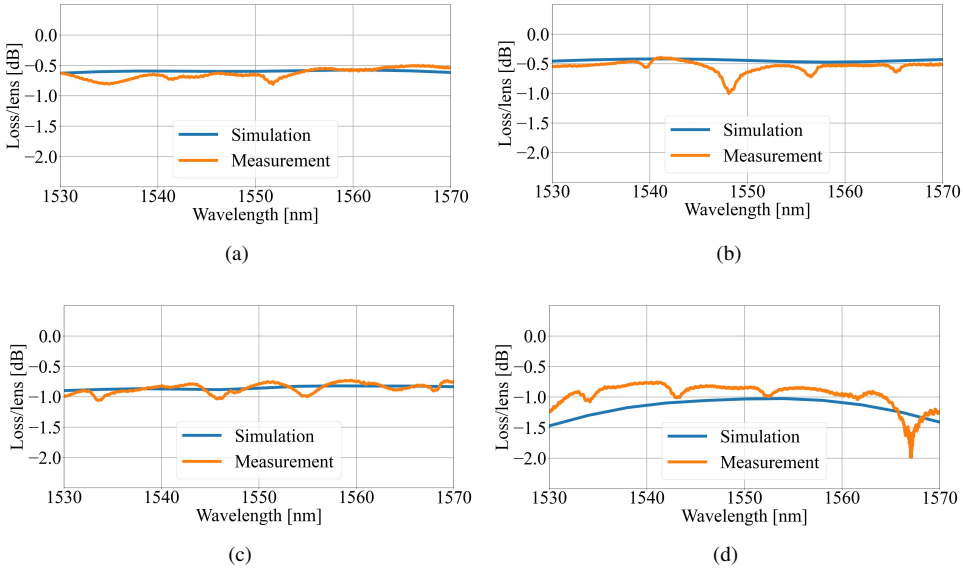

Fig. 11. Insertion loss characterization for mode-size converters from a wide to a narrow waveguide: (a) singlet, from 9.5 µm to 0.5 µm, length of 8 µm, (b) singlet, from 9.5 µm to 0.5 µm, length of 11 µm, (c) singlet, from 15 µm to 0.5 µm, length of 15 µm, (d) doublet, from 15 µm to 0.5 µm, length of 10 µm.

3.3. Payload measurements

The effect of silicon photonics devices on high-speed signal integrity is an important metric for actual data transmission. To investigate this aspect, we extracted the eye diagrams for non-return to zero (NRZ) encoding (PRBS pattern 2^{31}-1) at transmission rates of 32 Gbit/s, 40 Gbit/s and 50 Gbit/s for the two singlets (taper lengths of 8 µm and 15 µm) and the doublet. It is important to differentiate between the signature of the test-bed (Fig. 12) and those of the devices. For instance, our RF driver is limited to a transmission rate of 50 Gbit/s. Therefore, we characterized a device-less loopback, which served as a baseline reference (Table 1). Fig. 13 shows very minor changes in the eye openings for all the devices investigated. Table 2 shows that SNR changes of less than 10 % for all transmission rates, due to the presence of mode-size converters, are within the range of the measurement's accuracy (which corresponds to the peak-to-peak

Optics EXPRESS

voltage fluctuations). We can conclude that the metamaterial mode-size converters do not degrade the signal, and can be successfully used as devices in optical communication processing systems.

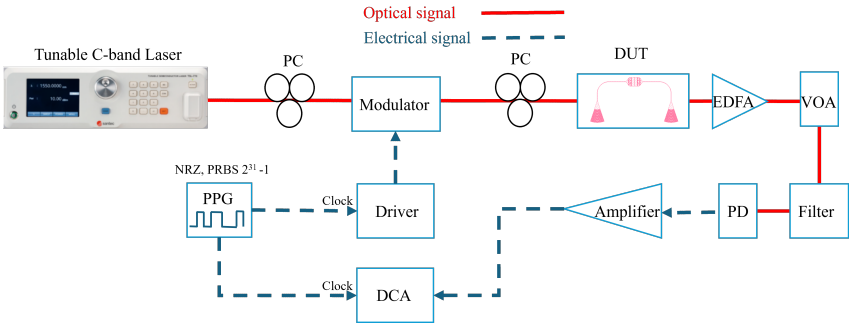

Fig. 12. High-speed measurement setup. PC: polarization controller, DUT: device under test, EDFA: erbium-doped fiber amplifier, VOA: variable optical attenuater, PD: photodiode, DCA: digital communication analyzer, PPG: pseudorandom pattern generator.

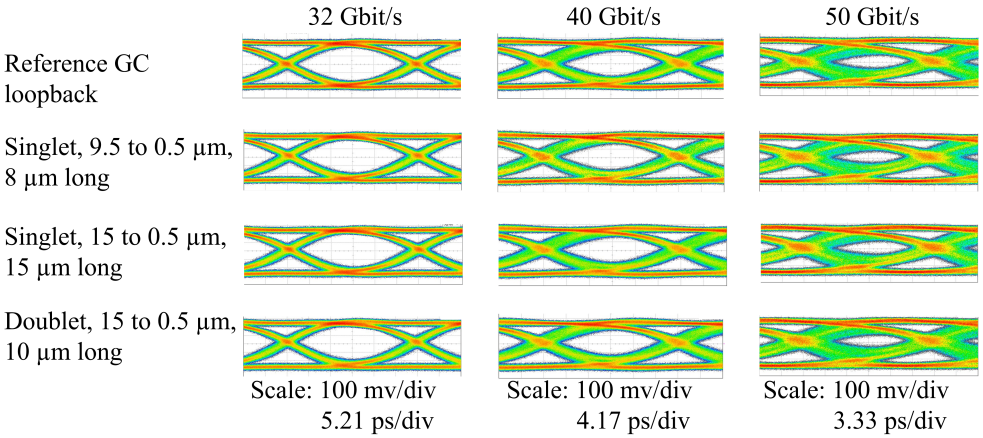

Fig. 13. Eye diagrams for different devices (rows) and data rates (columns). The variations compared to the reference are small.

Table 1. Baseline SNR of the reference loopback

SNR at 32 Gbit/s [dB]	SNR at 40 Gbit/s [dB]	SNR at 50 Gbit/s [dB]
10.94	6.28	3.73

Table 2. SNR change measurements relative to the GC loopback

Device	SNR change		
	at 32 Gbit/s [dB]	at 40 Gbit/s [dB]	at 50 Gbit/s [dB]
Singlet 8 um	-0.61	-0.01	-0.25
Singlet 15 um	-0.53	0.01	-0.01
Doublet	-0.72	-0.09	-0.26

Optics EXPRESS

4. Discussion and conclusion

The lens-assisted taper mode-size converters demonstrated high performance at a much shorter length compared to traditional adiabatic linear tapers. This shows the potential of using free-space techniques, implemented by metamaterial slots as phase shapers, to significantly reduce the mode-size converter footprint. Using parameterized inverse design we can escape the limits imposed by local periodic approximation and enhance device performance. The short tapers can be useful in applications where a uniform GC is employed, such as the ones that require polarization diversity [26, 27] inputs, wherein long adiabatic tapers prevent high density integration. They can also appeal to applications where GCs are used as acquisition pixels [29].

This work adopted a fabrication-friendly approach that leveraged rectangular shaped slots rather than relying on the topological inverse design approach that can lead to irregular geometries [21]. The proposed geometry is more robust to random fabrication variations as well as superior in terms of insertion loss. For instance, in a comparable device that we fabricated, 8 μm-long light mode-size converter from a 9.5 μm-wide to 0.5 μm-wide waveguide, the insertion loss is at 0.8 dB over the C-band, while the topologically inverse designed device showed loss of more than 1 dB [21]. Also, our wavelength dependent loss over the C-band is only 0.15 dB compared to 1 dB in the cases of topologically inverse designed devices. Importantly for all the investigated singlets, the insertion loss and the wavelength-dependent loss is under the 1 dB and 0.25 dB marks, respectively, even for the more challenging example of the 15 μm to 0.5 μm-wide singlet. This highlights the benefits of physics driven parameterized design approach.

The doublet concept, which has been widely used in free-space optics, was applied to integrated taper using only 10 μm length, demonstrating a comparable performance at the peak wavelength to a 150 μm adiabatic linear taper. The insertion loss is near 1 dB for most of the C-band.

The payload measurements showed, at transmission rate of up to 50 Gbit/s (limit of our test-bed), that the metamaterial lenses maintain the signal integrity, validating their applicability in optical communication systems.

Ultimately, this work highlights that free-space optics concepts adopted for integrated photonics and coupled together with the parameterized inverse design can lead to clearly better devices. While the former provides a physically meaningful parameterization that is naturally fabrication-friendly, the latter uses general purpose Maxwell equation solver to mitigate the approximations taken at the initialization stage. The result is high performing, compact and reproducible devices like the ultra-short mode-size converters presented in this paper. This is a technological enabler for achieving compact wavefront manipulation functionality in a variety of silicon photonics applications.

Funding. National Research Council Canada (AI for Design challenge program); McGill University (The McGill University Engineering Doctoral Award); Jewish Community Foundation of Montreal (Jenny Panitch Beckow Memorial Scholarship Canada).

Disclosures. The authors declare that there are no conflicts of interest related to this article.

Data availability. Data underlying the results presented in this paper are not publicly available at this time but may be obtained from the authors upon reasonable request.

References

1. S. Shekhar, W. Bogaerts, L. Chrostowski, *et al.*, "Roadmapping the next generation of silicon photonics," Nat. Commun. **15**(1), 751 (2024).
2. S. Y. Siew, B. Li, F. Gao, *et al.*, "Review of silicon photonics technology and platform development," J. Lightwave Technol. **39**(13), 4374–4389 (2021).
3. P. L. McMahon, "The physics of optical computing," Nat. Rev. Phys. **5**(12), 717–734 (2023).
4. H. Zhou, C. Zhao, C. He, *et al.*, "Optical computing metasurfaces: applications and advances," Nanophotonics **13**(4), 419–441 (2024).
5. D. Taillaert, F. V. Laere, M. Ayre, *et al.*, "Grating couplers for coupling between optical fibers and nanophotonic waveguides," Jpn. J. Appl. Phys. **45**(8R), 6071 (2006).

Optics EXPRESS

6. A. Fontbonne, H. Sauer, and F. Goudail, "Comparison of methods for end-to-end co-optimization of optical systems and image processing with commercial lens design software," Opt. Express **30**(8), 13556–13571 (2022).
7. C. Kim, S.-J. Kim, and B. Lee, "Doublet metalens design for high numerical aperture and simultaneous correction of chromatic and monochromatic aberrations," Opt. Express **28**(12), 18059 (2020).
8. T. Stangner, T. Dahlberg, P. Svenmarker, *et al.*, "Cooke-triplet tweezers: more compact, robust, and efficient optical tweezers," Opt. Lett. **43**(9), 1990–1993 (2018).
9. P. Cheben, R. Halir, J. H. Schmid, *et al.*, "Subwavelength integrated photonics," Nature **560**(7720), 565–572 (2018).
10. J. M. Luque-González, A. Sánchez-Postigo, J. H. Hadij-ElHouati, *et al.*, "A review of silicon subwavelength gratings: building break-through devices with anisotropic metamaterials," Nanophotonics **10**(11), 2765–2797 (2021).
11. P. Cheben, J. H. Schmid, R. Halir, *et al.*, "Recent advances in metamaterial integrated photonics," Adv. Opt. Photon. **15**(4), 1033–1105 (2023).
12. Y. Zhao, J. Xiang, Y. He, *et al.*, "On-chip metamaterial enabled wavelength (de)multiplexer," Laser Photonics Reviews **16**(7), 2200005 (2022).
13. D. González-Andrade, J. G. Wangüemert-Pérez, A. V. Velasco, *et al.*, "Ultra-broadband mode converter and multiplexer using a sub-wavelength metamaterial," in (*2018 European Conference on Optical Communication (ECOC),*, vol. 2018), pp.1–3.
14. A. He, X. Guo, T. Wang, *et al.*, "Ultracompact fiber-to-chip metamaterial edge coupler," ACS Photonics **8**(11), 3226–3233 (2021).
15. M. Teng, B. Niu, K. Han, *et al.*, "Trident shape soi metamaterial fiber-to-chip edge coupler," in *Optical Fiber Communication Conference (OFC) 2019*, (Optica Publishing Group, 2019), p.Tu2J.6.
16. C. Pérez-Armenta, A. Ortega-Mo nux, J. M. Luque-González, *et al.*, "Polarization-independent multimode interference coupler with anisotropy-engineered bricked metamaterial," Photonics Res. **10**(4), A57–A65 (2022).
17. H. Shiran, G. Zhang, and O. Liboiron-Ladouceur, "Dual-mode broadband compact 2 × 2 optical power splitter using sub-wavelength metamaterial structures," Opt. Express **29**(15), 23864–23876 (2021).
18. H. Xu, Y. Qin, G. Hu, *et al.*, "Compact integrated mode-size converter using a broadband ultralow-loss parabolic-mirror collimator," Opt. Lett. **48**(2), 327–330 (2023).
19. C. Pérez-Arancibia, R. Pestourie, and S. G. Johnson, "Sideways adiabaticity: beyond ray optics for slowly varying metasurfaces," Opt. Express **26**(23), 30202–30230 (2018).
20. M. Zhelyeznyakov, J. Fröch, A. Wirth-Singh, *et al.*, "Large area optimization of meta-lens via data-free machine learning," Communications Engineering **2**(1), 60 (2023).
21. W. Ma, M. Hou, R. Luo, *et al.*, "Topologically-optimized on-chip metamaterials for ultra-short-range light focusing and mode-size conversion," Nanophotonics **12**(6), 1189–1197 (2023).
22. Z. Wang, T. Li, A. Soman, *et al.*, "On-chip wavefront shaping with dielectric metasurface," Nat. Commun. **10**(1), 3547 (2019).
23. D. Vercruysse, N. V. Sapra, L. Su, *et al.*, "Analytical level set fabrication constraints for inverse design," Sci. Rep. **9**(1), 8999 (2019).
24. A. Michaels and E. Yablonovitch, "Leveraging continuous material averaging for inverse electromagnetic design," Opt. Express **26**(24), 31717–31737 (2018).
25. C. Zhu, R. H. Byrd, P. Lu, *et al.*, "Algorithm 778: L-bfgs-b: Fortran subroutines for large-scale bound-constrained optimization," ACM Trans. Math. Softw. **23**(4), 550–560 (1997).
26. Y. Xue, H. Chen, Y. Bao, *et al.*, "Two-dimensional silicon photonic grating coupler with low polarization-dependent loss and high tolerance," Opt. Express **27**(16), 22268–22274 (2019).
27. W. Bogaerts, D. Taillaert, P. Dumon, *et al.*, "A polarization-diversity wavelength duplexer circuit in silicon-on-insulator photonic wires," Opt. Express **15**(4), 1567–1578 (2007).
28. T. Watanabe, B. I. Bitachon, Y. Fedoryshyn, *et al.*, "Coherent few mode demultiplexer realized as a 2d grating coupler array in silicon," Opt. Express **28**(24), 36009–36019 (2020).
29. F. Ashtiani, A. J. Geers, and F. Aflatouni, "An on-chip photonic deep neural network for image classification," Nature **606**(7914), 501–506 (2022).